Correlated magnetic noise across Virgo and spatially separated gravitational-wave detectors

VIR-0364A-15

Melissa Guidry[1*], Irene Fiori[2], and Federico Paoletti[2]

[1] *College of William and Mary, Williamsburg, Virginia 23187, USA*
[2] *EGO - European Gravitational Observatory*

Date: August 20, 2015

[*] *corresponding author:* maguidry@email.wm.edu

Contents

1 Introduction

Gravitational-waves (GWs) have long been known to exist since their indirect detection by Hulse and Taylor in 1975 [1]. By accurately measuring the change in period of a pulsar in a binary system, it has been predicted that the two objects will eventually in-spiral toward each other partly due to the radiation of GWs. Direct observation of GWs using earth-based interferometeric detectors would provide a new window for astrophysics and test current theories of gravitation. The most sensitive of these detectors include EGO's Virgo (Pisa, Italy) and LIGO (Hanford, Washington and Livingston, Lousiana). The detectors are currently upgrading to ten-fold better sensitivity (Advanced Virgo (AdV) and Advanced LIGO (aLIGO)), with the first joint data taking foreseen for 2016 [2].

GW astronomy hopes to measure the stochastic gravitational-wave background (SGWB), which arises from a large number of random, independent events combining to form an isotropic signal. In cosmological models as opposed to astrophysical, the SGWB may be created from inflationary physics [3][4][5][6], cosmic strings [7][8], and pre-big-bang physics [9][10]. Its detection may allow a probe into the earliest moments after the big-bang [6].

The search strategy for the SGWB is to cross-correlate strain data channels from at least two detectors. By performing a year-long integration of data, it is possible to increase sensitivity to signals that would normally be masked by strain noise. A key assumption in this technique is that the noise in each detector is uncorrelated. Uncorrelated noise is reduced with continued integration whereas correlated noise is not, producing a systematic bias. A low level of correlated noise is best achieved in spatially separated detectors where local noise sources are not shared. However, global electromagnetic (EM) fields are a source of correlated noise for such detectors. These fields may induce forces on magnets mounted directly on the test masses for position control (such as in initial Virgo, initial LIGO, and AdV) or on magnets higher up the test-mass suspension system (such as in aLIGO).

In our study, we focus on Schumann resonances: global EM resonances in the cavity formed by the surface of the Earth and the ionosphere. The cavity is excited by approximately 100 lightning strikes per second around the world, producing fields on the Earth's surface of $0.5 - 1.0$ pT $Hz^{-1/2}$ [11]. Observed over time, 10 pT bursts appear over a 1 pT background [12], at a rate of ≈ 0.5 Hz. The primary resonance is at 7.8 Hz, with secondary and tertiary resonances at 14.3 Hz and 21.8 Hz respectively. The amplitudes and peak frequencies vary slightly with proximity to lightning strikes and exhibit a spectral width of $\approx 20\%$ (where spectral width is the full width at half maximum of the peak divided by the central frequency).

Previously, magnetic field data have been taken using magnetometers housed in the Virgo and LIGO observatories. Averaged over three months, coherence peaks were found at the known Schumann resonance frequencies on the order of 10^{-4} [13]. Using measurements of the coupling between magnetic fields and initial LIGO test mass motion, the level of correlated strain noise present in initial LIGO SGWB analyses has been inferred. The amount of coupling at which correlated noise becomes comparable to expected SGWB sensitivity has been estimated, and we now strive to meet the magnetic isolation specifications.

EM-induced correlated noise may be reduced by minimizing magnetic coupling to the strain channel through the removal of magnetic components. For example, smaller sized magnetic actuators will be used in the AdV upgrade. However, it is unclear whether second-generation detectors will be capable of achieving sufficient magnetic isolation to avoid limiting our SGWB search capabilities. An alternative method is to use magnetometers to subtract correlated noise, where a Wiener filter scheme may be implemented. Effective subtraction requires precise measurement of global EM fields near detectors of interest. This demands low local EM contamination around the measurement station.

In this paper we report on measurements of global EM fields at electromagnetically quiet locations in and around the Virgo detector site.

2   Formalism

2.1   Schumann formula

Our planet may be modeled as a solid conducting sphere surrounded by a thin dielectric atmosphere [14]. The thickness of the air layer is small in comparison to the Earth's radius $a \approx 6400$ km. The conductivity of air increases by six orders of magnitude when ascending toward the ionosphere.

The lower parts of the atmosphere are like a thin dielectric layer located between two conductors, the plasma of the ionosphere and the Earth's surface. Thus, a cavity with the properties of a spherical waveguide is formed. When the wavelength of EM waves in the cavity becomes on the order of the Earth's circumference $\lambda \approx 2\pi a$, a global resonance may occur [14].

Natural Schumann resonance excitation is mostly caused by lightning discharges. Lightning discharges radiate EM energy at frequencies below 100 kHz [15]. These signals are very weak as the distance from the discharge grows, but the waveguide behaves like a resonator at extremely low frequencies.

In an ideal cavity, the resonant frequency of the n-th mode f_n is determined by the Schumann formula [16]:

$$f_n = \frac{c}{2\pi a}\sqrt{n(n+1)}. \tag{2.1}$$

For the Earth-ionosphere cavity particular resonances are: $f_1 = 10.6$, $f_2 = 18.3$, and $f_3 = 25.9$ Hz. The observed peak frequencies are lower than those predicted by the Schumann formula. This is because the real Earth-ionosphere waveguide is not a perfect EM resonant cavity. The observed peaks are lower in frequency and structurally wide, with a quality factor Q ranging from 4 to 6, attributed to finite conductivity of the lower ionosphere [14]. Theories have since been adapted to account for the observed peak qualities.

We may distinguish Schumann resonances by taking the discrete time signal from a magnetometer and looking at how the power of the time series is distributed with frequency. While the amplitudes and peak frequencies are known to vary slightly, distinct structures are observed around the nominal peak frequencies in the frequency domain.

2.2   Converting ADC output

For each sensor, the data we want to analyze are measured in Volts at the input of the analog-to-digital converter (ADC) where they are converted into binary bits. The first scaling factor applied to the raw data is the conversion from bits back to Volts. If the data arrive as binary signed integers, they are converted to floating-point numbers by multiplication with the factor

$$V_{LSB} = \frac{V_{max} - V_{min}}{2^n}, \tag{2.2}$$

where V_{LSB} is the voltage corresponding to a least significant bit, V_{max} is the ADC maximum input voltage, and n is the number of bits of the ADC. Generally, $V_{min} = -V_{max}$. We then scale our data by a sensor-specific calibration constant, from Volts to the corresponding physical unit. We thus have a time series of equidistant samples to be processed.

Our sensors record data at a fixed sampling frequency f_s. If a discrete Fourier transform (DFT) is computed on an N-sample long signal, the width of a frequency bin, also called frequency resolution, is given by

$$f_{res} = \frac{f_s}{N}. \tag{2.3}$$

From the Nyquist theorem [17], it follows that the maximum useful frequency is exactly half of the sampling frequency. Thus we obtain $N/2$ frequency bins of the width f_s/N in the output.

2.3   Spectral density and coherence

We use the sequence of time samples of the digitized signal to calculate the power spectral density (PSD). The PSD describes how the squared amplitude of a signal is distributed with frequency. We then take the square root of the power spectral density to calculate the amplitude spectral density (ASD). The ASD is often used because it can be directly related to the parameters of the experiment [18].

We define our PSD for channel x to be

$$P_x(f) = \frac{|\widetilde{s_x}|^2}{\mu}, \tag{2.4}$$

and our cross-PSD for channels x and y to be

$$P_{xy}(f) = \frac{\widetilde{s_x}\widetilde{s_y}^*}{\mu}, \tag{2.5}$$

where $\widetilde{s_x}$ is the DFT for channel x and μ is a discrete Fourier transform normalization constant (see Appendix A, Eq. A.5). Finally, we define coherence between the two channels to be

$$coh(f) = \frac{|\overline{P_{xy}(f)}|^2}{P_x(f)\ P_y(f)}. \tag{2.6}$$

The overline denotes time-averaging over N segments. If s_x and s_y are independent, Gaussian, and stationary random variables, then $\langle coh(f) \rangle = 1/N$ [13]. Deviations from this value are evidence that one of these three assumptions is violated. This is useful for determining if two channels are correlated. For a full derivation of these concepts and their implementation, see Appendix A.

2.4   Wiener filtering

Wiener filtering is used to subtract noise from a main channel using a witness channel when the transfer function from witness to main is not known *a priori* [19]. In our case, the strain channel s acts as the main whereas a magnetometer channel w acts as the witness. Given two witness sensors w_1 and w_2 for detecting correlated magnetic noise m in two strain channels s_1 and s_2,

$$\begin{aligned} w_1(t) &= m(t) + \eta_1(t), \\ w_2(t) &= m(t) + \eta_2(t). \end{aligned} \tag{2.7}$$

The *eta* terms represent noise in each witness sensor, either electronic or from local magnetic fields. This noise is uncorrelated between the two witness sensors.

The witness-to-main transfer functions are estimated to be

$$\begin{aligned} \hat{r_1}(f) &= \frac{\overline{\widetilde{s_1}(f)\widetilde{w}_1^*(f)}}{\overline{\left|\widetilde{w}_1(f)\right|^2}}, \\ \hat{r_2}(f) &= \frac{\overline{\widetilde{s_2}(f)\widetilde{w}_2^*(f)}}{\overline{\left|\widetilde{w}_2(f)\right|^2}}. \end{aligned} \tag{2.8}$$

4

The hats are used to denoted estimated quantities. Thus, the Wiener-subtracted strain data are given by

$$\widetilde{s}'_1(f) = \widetilde{s}_1(f) - \hat{r}_1(f)\widetilde{w}_1(f),$$
$$\widetilde{s}'_2(f) = \widetilde{s}_2(f) - \hat{r}_2(f)\widetilde{w}_2(f).$$

(2.9)

Here s'_1 and s'_2 are referred to as the "cleaned" channels. In the limit where the estimated transfer functions equal the real transfer functions, the correlated noise goes to zero and the subtraction is perfect [19].

In practice, this is not the case. As the witness sensor noise grows larger than the correlated noise, the estimation of the transfer function deviates more from reality. With larger deviation, Wiener filtering fails. Thus we can determine the success of our estimation, and thus our filter, using the "witness signal-to-noise ratio"

$$\rho_w^2(f) = \frac{M(f)}{\mathcal{N}(f)},$$

(2.10)

where M is the cross-power of m_1 and $\mathcal{N}(f)$ is the PSD of the witness sensor noise. For a witness signal, $\rho_w(f)$ must be sufficiently high in order to provide successful Wiener filtering. This ratio may be qualitatively assessed as the resolution of the Schumann resonances in the frequency domain of the witness channel. For more information, see Ref. [19].

3 Procedure and results

3.1 Experimental setup

The data acquisition system (DAQ) utilized a low-noise coil-based magnetometer and a three-axis seismometer. A digital recorder with time-stamp capabilities was used for long-term measurements and a spectrum analyzer was used for short-term measurements.

Metronix MFS-06 magnetometers were used for all magnetic measurements. This sensor utilizes a sensor coil consisting of a high permeable ferrite core and several thousand copper turns. The magnetometer outputs a voltage signal, proportional to magnetic flux through the coil.

This magnetometer may function in two modes, "chopper on" and "chopper off". The "chopper on" mode of operation is used to reduce low frequency sensor noise due to thermal drifts. The two different modes allow frequency sensitivities of 0.00025 to 500 Hz and 10 Hz to 10 kHz, respectively. The output sensitivity varies with respect to the frequency. The sensitivity function was measured and used in subsequent conversions from Volts to Tesla (see Appendix B, Fig. 11). Neither chopper mode increased resonance resolution because the sensitivity increase is all below 1 Hz. For our first off-site quiet standard measurements, we operated with the chopper off. However, in order to better investigate low frequency noise sources, we turned the chopper on for on-site measurements. The nominal noise floor from the specifications was used for ASD comparison (see Appendix B, Fig. 12). In order to power the magnetometer with a ± 15 V source as specified, a custom DC-to-DC converter was used with a 38 Ah, rechargeable 12 V battery.

A Nanometrics Trillium seismometer was used with the magnetometer to investigate possible correlations between seismic activity and magnetic noise. Together, the two sensors output signals to a Nanometrics Centaur digital recorder during measurements spanning over multiple days. It consists of a 24-bit ADC, a GPS antenna receiver, and a 16 GB SD card for removable storage. A Crystal Instruments CoCo80 spectrum analyzer was used for short measurements. Unless otherwise specified, the sampling rate was set to $f_s = 250$ Hz with an input voltage range of $V_{max} - V_{min} = 4$ V.

It was essential that we limit low frequency noise $(1-20\,\text{Hz})$ at the installation in order to resolve our resonances. A common source of this noise is seismic vibrations of the equipment. These vibrations modulate the Earth's static magnetic field lines through the magnetometer as well as generate a magnetic field simply from moving

5

the metallic components (e.g. wires) within the vicinity. This noise was suppressed by either burying the sensors and their wires approximately 20 centimeters under the ground or placing the magnetometer inside a building. This setup also reduced thermal drifts within the seismometer but providing thermal insulation.

3.2 Quiet standard

In order to find a quiet location, "quietness" must first be defined. A location was deemed quiet if the Schumann resonances could be resolved by eye in the ASD plot without largely reducing the data set. The resolution of Schumann resonances is indicative of a high ρ_w, whereas a location is more efficient if less data are discarded. A location with a duty cycle of 25% is desired (N. Christensen, personal communication, June, 2015).
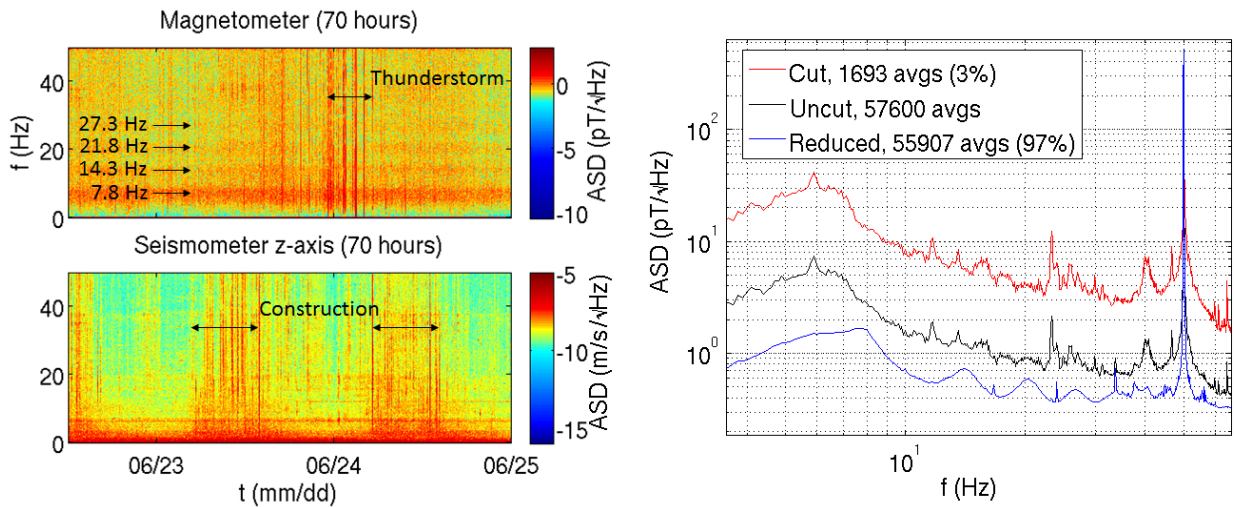
Figure 1: Left: Magnetic and seismic spectrograms at Villa Cristina between June 22-25 2015. The first four Schumann resonances are observed in the magnetometer spectrogram. Glitches within both spectrograms are identified. Right: Five Schumann resonances (7.8, 14.3, 20.8, 27.3, and 33.8 Hz) are clearly resolved after cutting only 3% of 160-hours-worth of Villa Cristina data from June and July 2015. The black line is the full set of averaged ASDs. The red line is the average of the ASDs that are removed from the set. The blue line is the average of the set after the less quiet ASDs are removed.

The data are reduced using a post-processing selection that removes extraordinarily large increases in magnetic noise that are transient in nature, known as glitches. A data set consists of a time-series of 10-second-long ASDs between 0 Hz and the Nyquist frequency. The filter uses a cutting threshold, typically taken as the average ASD value across the entire time period and across the 10-30 Hz frequency range. This frequency range was chosen because, for individual ASD plots, small average amplitudes in this range proved to be most indicative of resolvable Schumann resonances. The ASDs where the average amplitude value in the 10-30 Hz range is above the threshold are then removed. The threshold may be lowered until the resonances are resolved or statistics become too low.

Before testing on-site locations, we measured a quiet standard which would act as a lower limit for future comparisons. This was the average of 160 hours worth of data taken inside Villa Cristina, a scout house located 13 km South-West of Virgo in the Livorno Hills (for a picture of the surrounding environment, see Appendix C, Fig. 13). These data were collected June 22 to June 25, and June 29 to July 3 (all weekdays). The magnetometer and seismometer were placed inside the scout house with the magnetometer length and seismometer y-axis oriented North-South.

Spectrograms for 70 hours worth of Villa Cristina data are shown to the left in Fig. 1. The first four Schumann resonances are observed as broad bands across the entire time window. In the magnetometer spectrogram,

a specific set of glitches were attributed to a thunderstorm by looking at coincidences with a Virgo-based lightning counter. Magnetic glitches were more common during daylight hours, attributed to the movement of heavy metal machinery cutting down trees in the area during this time. This source is observed as periodic stretches of glitches in the seismometer spectrogram. Despite this noise, the first five Schumann resonances were clearly resolved after cutting only 3% of data using the aforementioned cutting procedure (see Fig. 1, right). The Villa Cristina site exhibited high efficiency at a potentially high ρ_w value.

The transfer function between seismic activity and local magnetic noise was not assumed to be linear. However, as a preliminary exploration of the coupling, the coherence was calculated between the seismometer channels and the magnetometer channel. In Fig. 2, the coherence is calculated between the magnetometer and each of the seismometer axes for the first 70 hours of uncut data. In the uncut magnetometer average ASD plot, three peaks were evident at 26, 35, and 37.8 Hz. In the coherence plot, we see coherence peaks at these same frequencies.
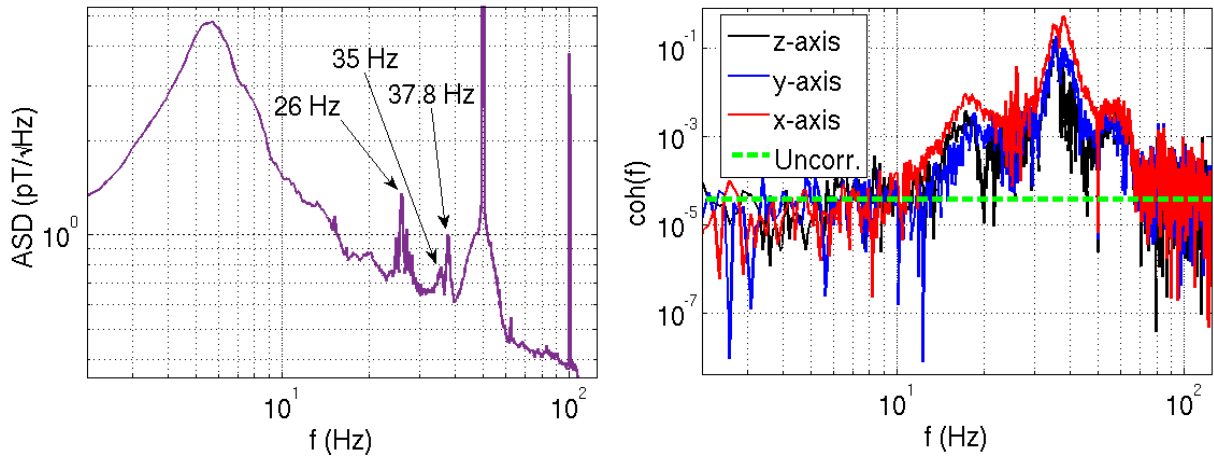

Figure 2: Left: Magnetometer ASD plot for 70 hours worth of uncut Villa Cristina data, collected June 22-25. Noise peaks have been distinguished with arrows. Right: Coherence between the magnetometer and three axes of the seismometer data over 70 hours. The dashed green line represents the average level of uncorrelated noise.

The largest coherence was found at 37.8 Hz for the x-axis of the seismometer. To better understand the correlation, the ASD values in the time domain were plotted for this peak frequency in Fig. 3. We see a periodic increase in seismic and magnetic activity stretching from 5:00 to 12:00 UTC each day. Here we attribute this to the tree removal in the area at these times. The largest central peak in the magnetometer data (purple) occurred during a thunderstorm, and thus does not seem to fit the periodic pattern or appear as strongly in the seismic data. We conclude that the three noise peaks in the uncut 70-hour magnetic average ASD plot are either fully or partially seismically induced. It is important to note that the ρ_w value for this location, as well as future stations, will vary depending on the level of seismic activity.
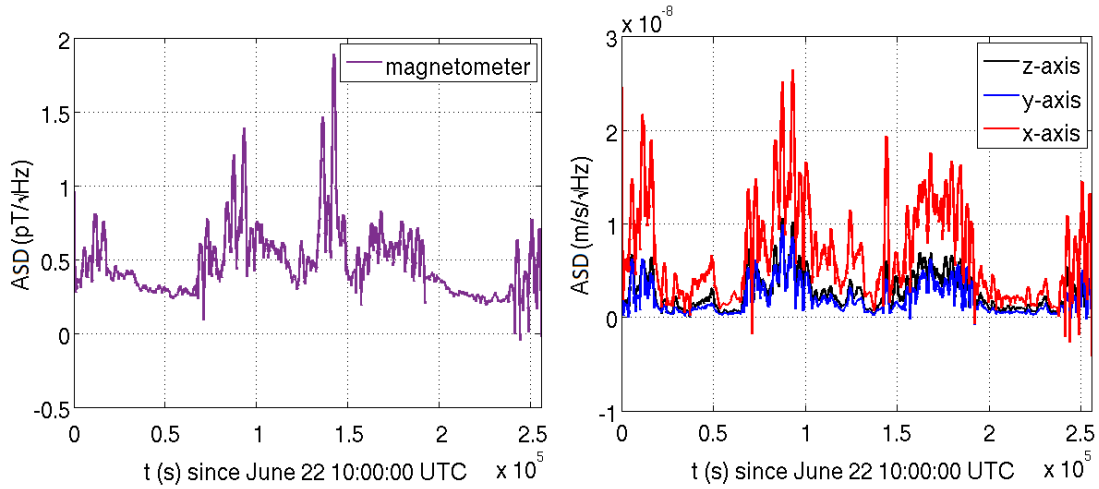
Figure 3: ASD values over time for 37.8 Hz. Left: The magnetometer data. Right: The seismometer x-, y-, and z- axes data.

The coherence was also calculated between the Villa Cristina data and data from magnetometers housed in the LIGO Hanford Observatory (LHO). The LHO magnetometers with the smallest noise were used for the full 160-hour comparison. These were found to be the three axes of the "H1:PEM-CS" setup, near the vertex of the main LHO interferometer (see Appendix C, Fig. 14 for a picture of the surrounding environment). It is observed that the LHO magnetometer noise is about one order of magnitude above the Schumann peaks (see Fig. 4).
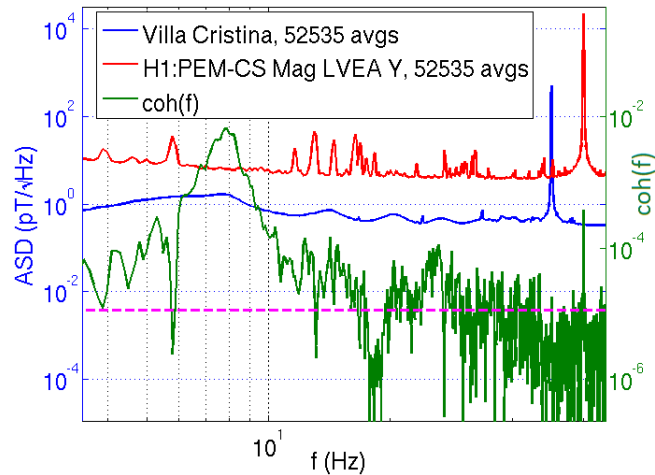
Figure 4: Left: Coherence between Villa Cristina and the LHO H1:PEM-CS y-axis magnetometer (green line). The purple dashed line indicates the average coherence value expected for uncorrelated noise. These two lines are plotted with respect to the right vertical axis. The average clean ASDs (red and blue) are plotted with respect to the left vertical axis. Right: 15 locations along the Virgo arms where EM measurements were conducted. All measurements were done between June and July 2015.

All three magnetometers were coherent at two main frequencies. We see a broad peak characteristic of Schumann resonance coherence at 7.8 Hz, as well as a narrow peak characteristic of electrical noise at exactly 60 Hz, the mains frequency of the United States (see Fig. 4). However, we saw insignificant coherence at 50 Hz, the mains frequency of Europe. This is most likely due to spectral leakage from the much larger amplitude of the 60

Hz component in the LHO magnetometer channels. In order to test that the 60 Hz coherence was a result of spectral leakage, we applied a numerical 60 Hz notch filter to the raw data of the LHO magnetometer. If the coherence was real, the coherence peak amplitude would not change. However, we saw the coherence peak reduce, allowing us to attribute the peak to spectral leakage.

Overlaying the coherence with the clean average ASDs between two of the magnetometers, the 7.8 Hz coherence peak exactly lines up with the primary resonance and there is no noise peak in the LHO ASD, providing good evidence that this is indeed Schumann induced. Previous Schumann resonance coherence analysis was done using magnetometers housed in the observatories at Virgo and the LHO [13]. These data were averaged over three months and resulted in a coherence at 7.8 Hz on the order of 10^{-4}. Using a week of Villa Cristina data, this coherence improved by nearly two orders of magnitude.

3.3   On-site location testing

Magnetic measurements were taken at different on-site locations (Fig. 5). These specific locations were chosen to avoid being close to electrical powerlines running over Virgo arms. Powerlines radiate magnetic noise, where the ASD plot in the band of interest consists of a prominent 50 Hz narrow peak. Often the 50 Hz noise is modulated, resulting in sidebands extending across other frequencies. An increase in the amplitude of the 50 Hz component typically results in an increase in the amplitude of this noise.
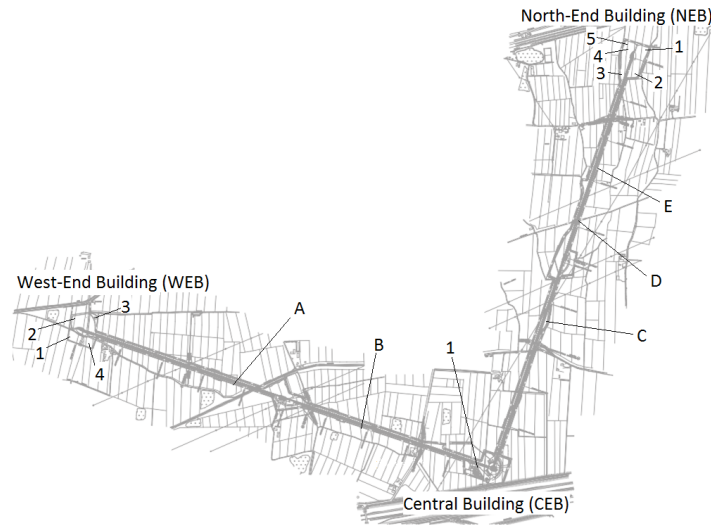

Figure 5: Virgo site: 15 locations along the detector where EM measurements were conducted. All measurements were done between June and July 2015.

Short measurements were taken using either the digital recorder or the spectrum analyzer, with the magnetometer axis oriented both magnetic North-South and East-West. An average ASD plot was generated for each site. Using the digital recorder, hours of clean data were averaged (sites Central Building (CEB) 1, North End Building (NEB) 1). Using the spectrum analyzer, minutes of data were averaged (sites West End Building (WEB) 1-4, A, B, C, D, E, NEB 2-5).
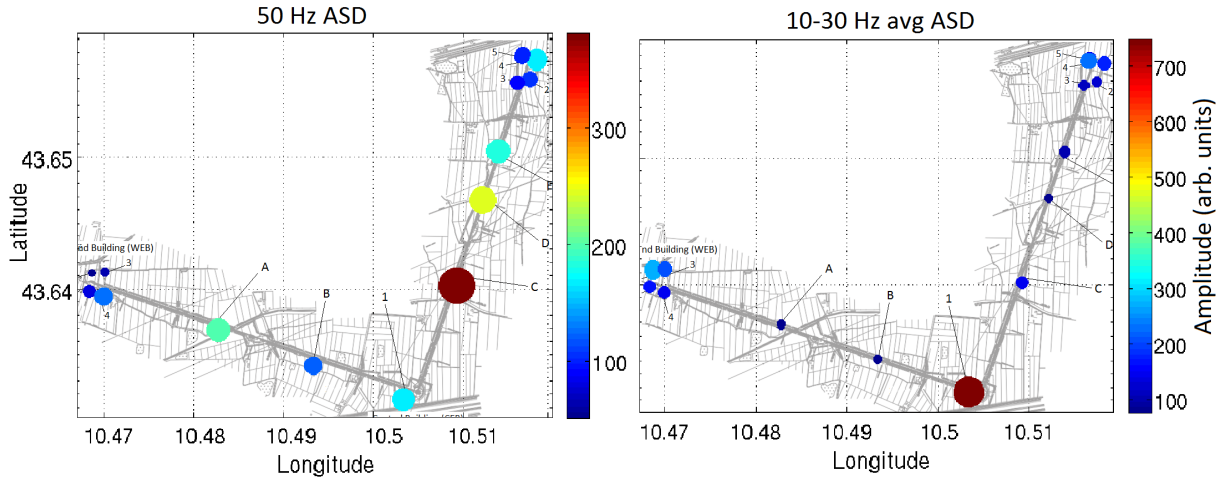
Figure 6: Left: 50 Hz ASD component for each location tested. Right: 10-30 Hz average ASD components.

At each location, two numbers were chosen for comparison: the ASD value at 50 Hz (Fig. 6, left) and the average ASD value between 10-30 Hz (Fig. 6, right). In Fig. 6, the size and color of the dot are both proportional to the ASD value (for exact values, see Appendix E, Table 1). We found that that the 50 Hz component was a decent predictor of how noisy a location may be, but it was the $10 - 30$ Hz average that was most indicative of noise that would obscure Schumann resonances. Site B had the smallest $10 - 30$ Hz average ASD value with the axis oriented East-West.

3.4 On-site quiet installation

A 14-day long installation was undertaken at Site B with the magnetometer and seismometer buried. Initial data analysis revealed three out of five main resonances resolved when cutting 35% of the data (see Fig. 7), well within the suggested duty cycle of 25%. However, on the second day of data collection the measurements became contaminated by local magnetic noise. This noise appeared in the form of 0.5 Hz sidebands around the 50 Hz component. When analyzing a time where sidebands were always on, no matter how extensive the cutting the resonances were unresolvable (see Appendix D, Fig. 15).
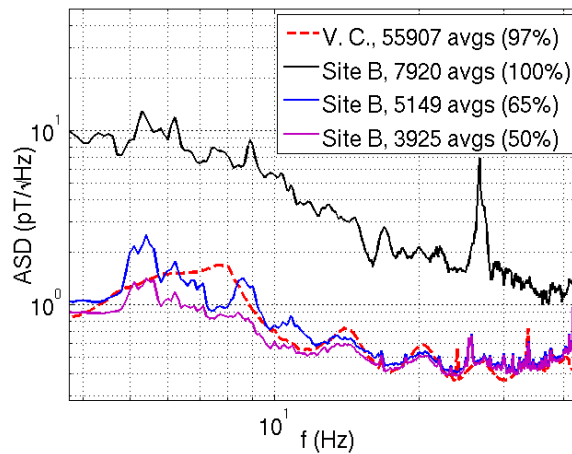

Figure 7: Site B: Three out of four main Schumann resonances were resolved after cutting only 35% of data. 22 hours of data were taken between July 16-17, 2015.

A 230 kV powerline running over the West Virgo arm was predicted as the source. Four electrical powerlines run over the Virgo site. Each one was investigated by measuring directly underneath with a small size tri-axial flux gate FL3-100 magnetometer and the spectrum analyzer. A diagram of the powerlines (right) tested as well as their respective magnetic ASD plots (left) is shown in Fig. 8.
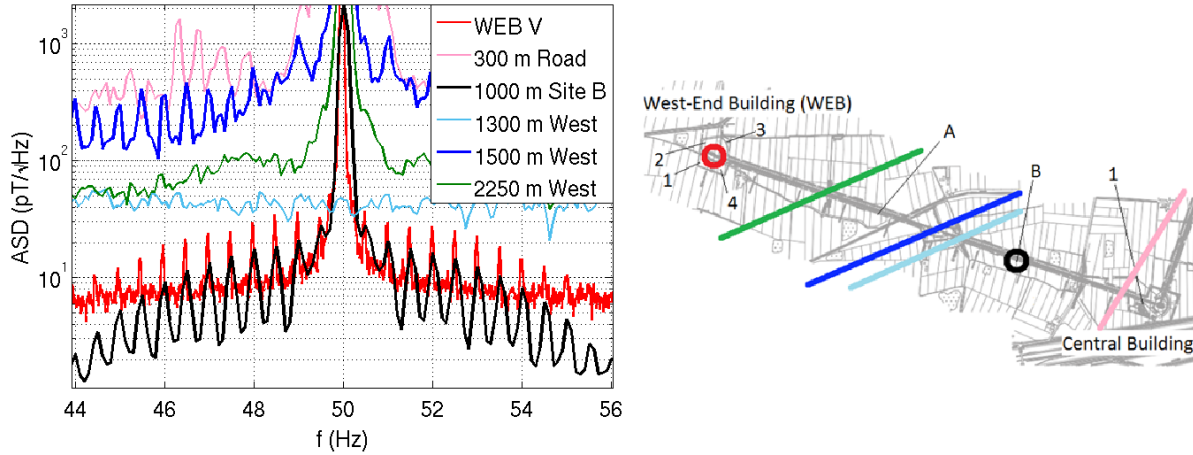

Figure 8: Left: Average ASDs for surveys done under power lines, as well as for the Site B and WEB (vertical) magnetometers. The 0.5 Hz sideband noise is present at Site B (black), WEB (red), and the 230 kV power line (dark blue). All ASDs were generated with the same frequency resolution except for the WEB, where a higher frequency resolution is used. Right: A map relating different ASD plot lines (colors) to different powerline sites tested.

Two lines showed signs of sidebands: 300 m down the road from Virgo (pink) and 1500 m down the West Arm (dark blue). However, it was the 1500 m line that seemed to display 0.5 Hz sidebands consistent with the Site B installation (black line). This is a 230 kV line which runs across both interferometer arms.

Further measurements revealed that the sidebands were only visible in the ASD plot when the measurement was taken next to the door of the West tunnel, which happened to be our first and most convenient measuring location. Measurements along the outside of the West tunnel revealed that the 0.5 Hz sideband noise was only present when next to tunnel doors. Investigating inside the tunnel, we found increased amplitudes of the sidebands next to various electrical wires. While we are still hunting for the 0.5 Hz sideband source, this analysis provides evidence that the source is internal to Virgo.

It was observed that the WEB magnetometers displayed a sensitivity to the 0.5 Hz sidebands as well (red), with the vertical magnetometer being particularly sensitive. Coherence was calculated between the WEB magnetometers and the Interruptible Power Supply (IPS) monitors. At sideband frequencies, no coherence was found.

A spectrogram was generated between 45 and 50 Hz spanning back to February using WEB vertical magnetometer data (see Fig. 9) in order to see if the 0.5 Hz sideband noise had occurred previously. The dark blue block represents a period when data collection was temporarily offline. The first sideband noise event was observed on July 7 2015 at about 16:19:12 UTC. Since then, the sideband noise has turned on and off without a clear pattern in time.
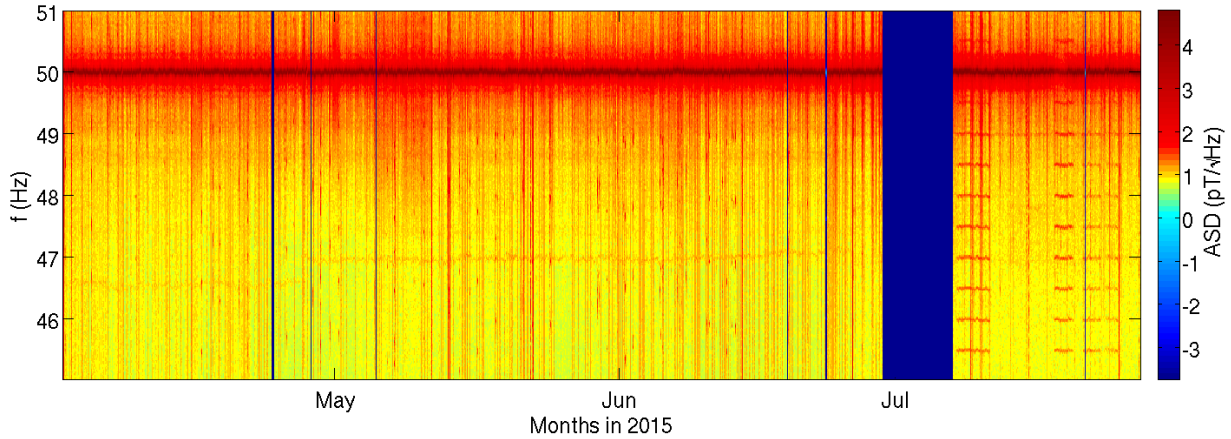
Figure 9: A spectrogram using WEB vertical magnetometer data dating back several months to look for sideband noise emergence. We determine that the sideband noise is a recent feature.

On June 26 2015, we noticed that our NEB magnetometers were saturating nearly 50% of the time because of a too intense 50 Hz magnetic signal. We relocated them in the building in order to reduce saturation. WEB magnetometers were not saturated but showed a very prominent noise bump at 14 Hz. We moved them in the building as well in an attempt to reduce this noise. Some magnetometers gained sensitivity during this time, which was right before we began to see the sideband noise in the WEB vertical magnetometer channel. It is unclear whether this sideband noise is newly occurring or if it was always present and our magnetometer simply was not sensitive enough to detect it.
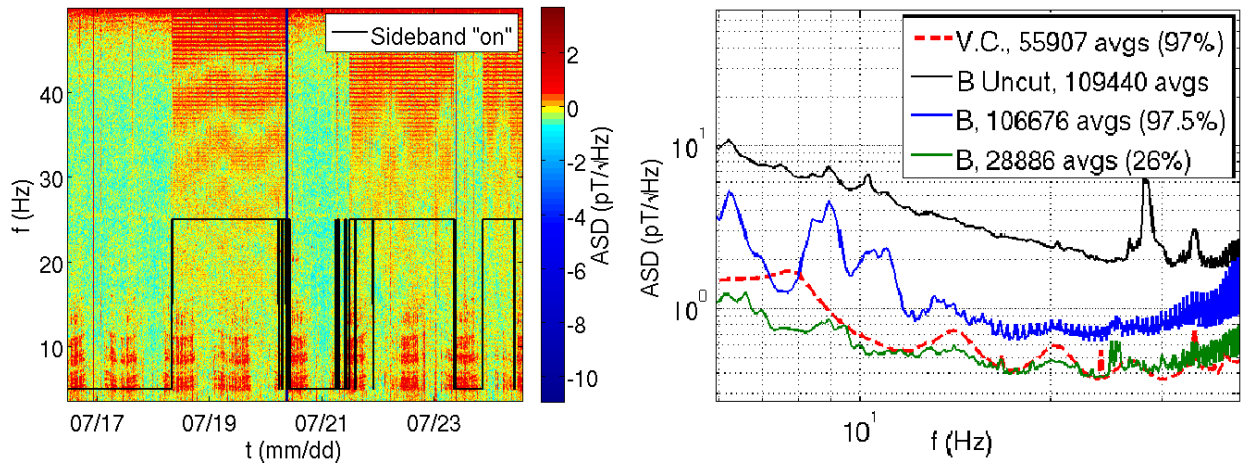

Figure 10: Left: A magnetic spectrogram for Site B displaying the sideband noise turning on and off. A digital count is overlaid with the plot (black line) which was used to determine the percentage of time the noise was present. Right: Site B ASD plot between July 16-30, the full time window for the installation. Cutting was done using thresholds averaged over $7 - 30$ Hz as opposed to $10 - 30$ Hz in order to better resolve the primary resonance. We see Schumann resolution at a duty cycle of 26%.

Between July 16-30, the sideband noise was present 45.1% of the time. This was determined by smoothing Site B ASD values at 45.5 Hz over the time window and determining if they went over a "sideband on" threshold determined through averaging. This frequency was chosen due to its relatively low noise levels during "sideband off" times and strong increase in power during "sideband on" times. In Fig. 10, left, the binary on-off counts have been overlaid with the Site B magnetometer spectrogram to demonstrate the sensitivity of the method.

12

This algorithm tends to work well when the sideband noise occurs for several hours and there are few glitches. Despite the smoothing, glitches with enough power will send the ASD value over the threshold, creating a false count. The smoothing also has the negative capability of ignoring a "sideband on" time that is very short (less then 3 hours) in duration. Most sideband noise occurrences are several hours in duration and high-power glitches are not frequent. Hence a $\pm 5\%$ error on the occurrence percentage may be assumed as a conservative estimate.

Without the sideband noise, Site B demonstrated a duty cycle of $\approx 65\%$. With the sideband noise on nearly half of the time, this duty cycle was significantly reduced. The Site B ASD data were averaged and cut for the full time window, which included both "on" and "off" times (see Fig. 10, right). Cutting was done using thresholds averaged over 7-30 Hz as opposed to 10-30 Hz in order to better resolve the primary resonance. We see Schumann resolution at a duty cycle of 26%. With optimized cutting, we predict that this value may be further increased. The lack of resolution of the primary resonance at 7.8 Hz continues to be investigated.

4   Implications

For successful Wiener filtering, Schumann resolution with a duty cycle of 25% is preferred. If the sideband noise persists, this duty cycle requirement is barely met at the Site B installation with rough cutting on the data set. With optimized cutting on the data set, this installation site may be well within the duty cycle requirement. If the sideband noise is understood and suppressed, the site will be further improved for long-term Schumann resonance resolution. Due to the internal nature of the source to the Virgo site, suppression is feasible.

The lack of resolution of the 7.8 Hz resonance is worth investigating but is not limiting for future filtering schemes. Our strain sensitivity is greater than 10 Hz and magnetic noise has been observed to couple linearly into the strain channel. The primary resonance will not be directly used for subtraction. It is the secondary and tertiary resonances that are most important for correlated noise subtraction and these are regularly resolved at Location B.

A permanent installation along the West Arm would require several modifications. A long-term power source would need to be realized as opposed to a rechargeable battery. This power could be drawn from the powerline along the arm and transformed into 12 V DC power in such a way as not to produce 50 Hz noise in proximity of the magnetometer. The data would need to be acquired continuously or at least automatically, without the use of a memory card. This could be realized in the form of an ADC board which streams data to the main Virgo DAQ system (which utilizes the main GPS clock) using ethernet wires. Cables would need to stretch across the road between the sensors and the West arm, and this may require digging a small ditch under the road. Ideally, two more magnetometers could be utilized in order to measure along all three axes.

Once a permanent quiet magnetic station is established near Virgo, coherence may be measured with an upcoming quiet station near the LHO. Higher coherence over a short time is an indication of a high ρ_w in the witness sensors. Moving forward, the magnetic data will be used to test the success of different subtraction methods to determine which should be used for future science runs.

Acknowledgments

References

[1] R. A. Hulse, J. H. Taylor, "Discovery of a pulsar in a binary system", Astrophysical Journal, vol. 195 (1975). 2

[2] A. Krolak, "Advanced LIGO and Virgo projects" [PowerPoint slides]. Retrieved from http://acp15.fuw.edu.pl/talks/Krolak.pdf (2015). 2

[3] L.P. Grishchuk, Sov. Phys. JETP 40, 409 (1975). 2

[4] A. A. Starobinskii, JETP Lett. 30, 682 (1979). 2

[5] R. Easther and E.A. Lim, J. Cosmol. Astropart. Phys. 04 (2006) 010. 2

[6] M. Maggiore, Phys. Rep. 331, 283 (2000). 2

[7] R. R. Caldwell and B. Allen, Phys. Rev. D 45, 3446 (1992). 2

[8] T. Damour and A. Vilenkin, Phys. Rev. D 71, 063510 (2005). 2

[9] M. Gasperini and G. Veneziano, Astropart. Phys. 1, 317 (1993). 2

[10] V. Mandic and A. Buonanno, Phys. Rev. D 73, 063008 (2006). 2

[11] D.D. Sentman, in *Handbook of Atmospheric Electrodynamics*, edited by H. Volland (CRC Press, Boca Raton, 1995), Vol. 1, pp. 267-295. 2

[12] M. Füllekrug, J. Atmos. Terr. Phys. 57, 479 (1995). 2

[13] E. Thrane, N. Christensen, R. Schofield, Phys. Rev. D 87, 123009 (2013). 2, 4, 9

[14] A.P. Nickolaenko, M. Hayakawa, in *Resonances in the Earth-Ionosphere Cavity*, (Kluwer Academic Publishers, Dordrecht, 2002), Vol. 1, pp. 1-4. 3

[15] H. Volland. Atmospheric Electrodynamics. Springer-Verlag, Berlin (1984). 3

[16] W. O. Schumann, Zeitschrift und Naturforschung 7a, 149 (1952). 3

[17] H. Nyquist, "Certain topics in telegraph transmission theory", Trans. AIEE, vol. 47, pp. 617â644 (1928). 3

[18] G. Heinzel, A. Rüdiger, R. Schilling, "Spectrum and spectral density estimation by the Discrete Fourier Transform, including a comprehensive list of window functions and some new at-top windows", Albert-Einstein-Institute, Germany (2002). 4, 15

[19] E. Thrane, N. Christensen, R. Schofield, A. Effler, Phys. Rev. D 90, 023013 (2014). 4, 5

A   Full PSD definitions

The estimation of spectral densities is done using the discrete Fourier transform (DFT). The DFT takes a vector of N complex numbers s_k, $k = 0...(N-1)$, and transforms it into a vector of N complex numbers $\widetilde{s_m}$, $m = 0...(N-1)$ [18]. We define our DFT as

$$\widetilde{s_m} = \sum_{k=0}^{N-1} s_k \exp(-2\pi i \frac{mk}{N}), m = 0 \ ... \ N - 1. \tag{A.1}$$

Here s_k are defined as complex numbers, but the time series of the digitized input signal is always real.

The DFT assumes that the input is a finite data set with an integer number of periods, where the two endpoints of the time waveform are interpreted as though they were connected together. In practice, the measured signal is rarely an integer number of periods. The finite time signal then looks like a truncated waveform with different characteristics from the original continuous-time signal. This effect appears as sharp transition changes in the measured signal, which show up in the output as non-physical high-frequency components aliased between 0 and the Nyquist frequency. This is known as spectral leakage.

Spectral leakage may be minimized through windowing, where the amplitude of the discontinuities at the boundaries of each finite sequence are manually reduced. A window function to be used with a DFT of length N is defined by a vector of real coefficients w_k. It is used by multiplying the time series s_k with the window before performing the DFT. In our analysis, we use a Hanning window, defined as

$$w_k = \frac{1}{2}[1 - cos(\frac{2\pi \cdot k}{N})], k = 0 \ ... \ N - 1. \tag{A.2}$$

Finally, we may normalize our DFT results to generate our power spectrum (PS)

$$PS_{rms}(f_m) = \frac{2 \cdot |\widetilde{s_m}|^2}{\mathcal{C}_1^2}, m = 0 \ ... \ N - 1, \tag{A.3}$$

where $f_m = m \cdot f_{res}$ and $\mathcal{C}_1$ is the normalization constant

$$\mathcal{C}_1 = \sum_{k=0}^{N-1} w_k. \tag{A.4}$$

We may calculate our power spectral density (PSD, denoted P_x for the xth signal) by dividing the PS by the effective noise bandwidth

$$P_x(f_m) = \frac{2 \cdot |\widetilde{s_m}|^2}{f_s \cdot \mathcal{C}_2}, m = \ 0... \ N - 1, \tag{A.5}$$

where $\mathcal{C}_2$ is the normalization constant

$$\mathcal{C}_2 = \sum_{k=0}^{N-1} {w_k}^2. \tag{A.6}$$

For an amplitude spectral density (ASD), we simply take the square root of the corresponding PSD. However, this simple procedure described above tends to be noisy because the standard deviation of the spectrum estimate

in a frequency bin is equal to the estimate. Thus we take the average of M estimates and hence reduce the standard deviation of the averaged result by a factor of $1/\sqrt{M}$. This method of averaging several spectra while using a window function is also known as "Welch's method". In this report, all PSDs are calculated in this way.

If a time series is split into several non-overlapping segments of length N to be processed using a window function, we end up throwing out a large portion of the data stream. Some data are saved by letting the segments overlap. For the Hanning window, the recommended overlap is 50%, which is used throughout this report.

We must calculate the cross-power spectral density between the two data channels to find the coherence between them. For discrete signals s_x and s_y, we calculate the DFTs $\widetilde{s_x}$ and $\widetilde{s_y}^*$, where the latter is the complex conjugate of the DFT. Thus,

$$P_{xy}(f) = \frac{2 \cdot \widetilde{s_x}\widetilde{s_y}^*}{f_s \cdot \mathcal{C}_2},$$

(A.7)

where the coherence is then

$$coh(f) = \frac{|\overline{P_{xy}(f)}|^2}{\overline{P_x(f)}\ \overline{P_y(f)}}.$$

(A.8)
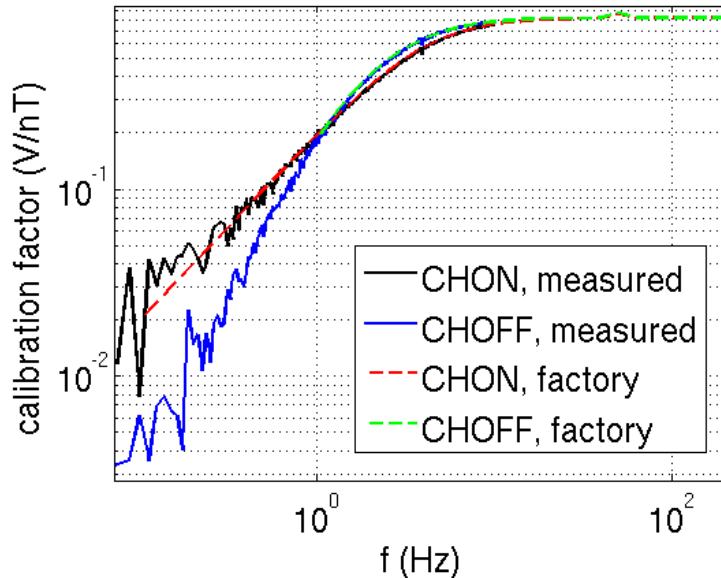
B Magnetometer specifications

Figure 11: The frequency-dependent calibration factor of the magnetometer MFS-06, with the chopper on (CHON) and off (CHOFF). This was measured by applying a known voltage and measuring the output voltage. This factor was then applied to subsequent measurements for accurate ASD comparisons.
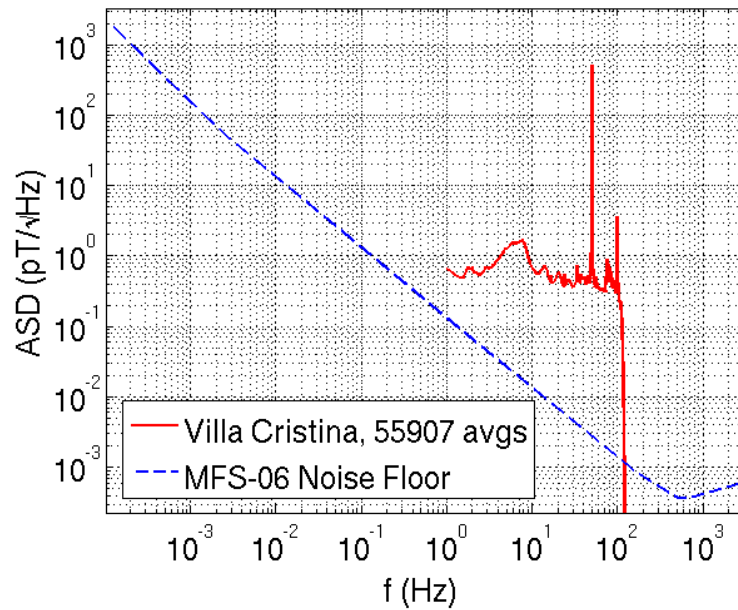
Figure 12: The MFS-06 nominal noise floor with Schumann resonances from Villa Cristina overlaid to demonstrate relative amplitude. It is well below all Schumann measurements and was thus excluded in plots in this report where the magnetometer was used.

C   Supplementary diagrams

Figure 13: The location of Villa Cristina (43.539625, 10.410031) in the Livorno hills. This site was specifically chosen due to its spatial separation from many sources of anthropogenic noise. Created using Google maps.
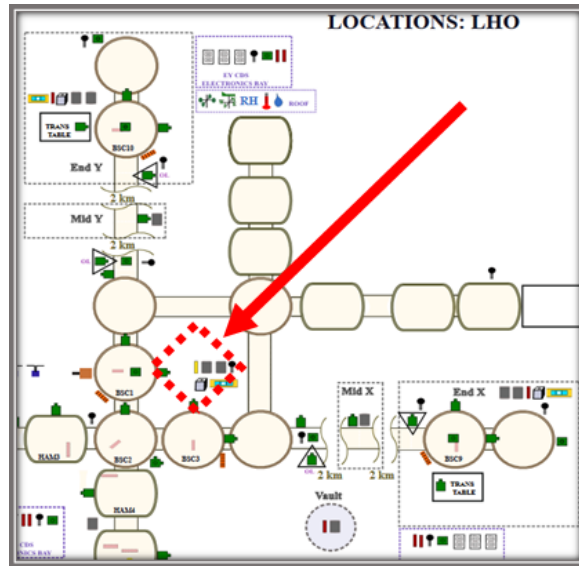
Figure 14: The location of the LHO magnetometers "H1:PEM-CS" used in our coherence analysis. The diagram was taken from the LIGO web-based data viewer, ligoDV-web (https://ldvw.ligo.caltech.edu/).

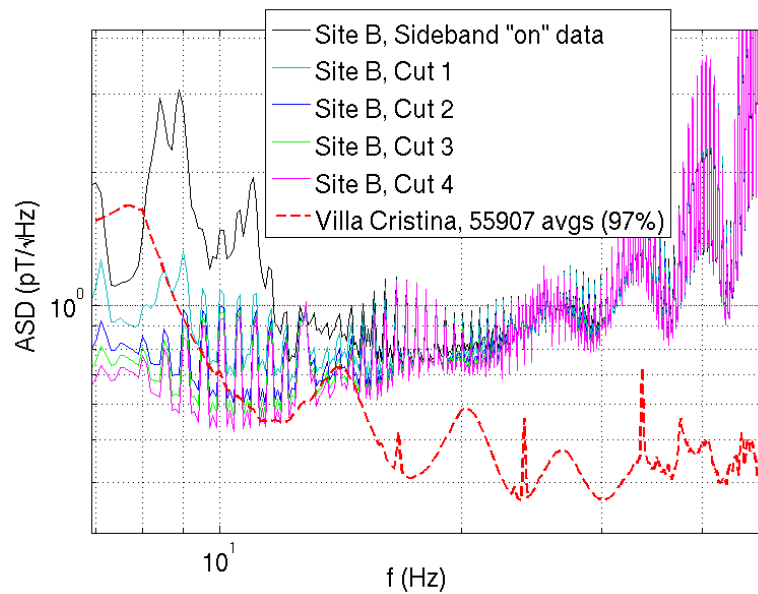# D   Supplementary figures

Figure 15: An ASD plot for Site B during a "sideband on" time is shown. No matter how much data are cut, the resonances are not resolvable.

E   Magnetic surveys

Loc./Or.	ASD(50 Hz)	ASD(10-30 Hz)
CEB 1 - EW	4082	6.247
NEB 1 - EW	4026	1.465
NEB 2 - EW	2099	1.027
NEB 3 - EW	1740	0.915
NEB 4 - EW	2047	1.884
NEB 5 - EW	2000	1.153
WEB 1 - EW	1391	1.345
WEB 2 - EW	535.1	2.256
WEB 3 - NS	918.4	1.68
WEB 4 - EW	2763	1.169
A - NS	4897	0.665
B - EW	2621	0.626
C - NS	10447	1.177
D - EW	6362	0.706
E - EW	4535	0.808

Table 1: A table with ASD values for different magnetic survey locations with the magnetometer orientations (North-South, NS; East-West, EW). The units for the ASD values are always $pT/\sqrt{Hz}$.